Contents lists available at ScienceDirect

Cement and Concrete Research

Predicting damage in aggregates due to the volume increase of the alkali-silica reaction products

E.R. Gallyamov [a,*], A. Leemann [b], B. Lothenbach [b,c], J.-F. Molinari [a]

[a] Civil Engineering Institute, Materials Science and Engineering Institute, École Polytechnique Fédérale de Lausanne (EPFL), Station 18, CH-1015 Lausanne, Switzerland
[b] Laboratory for Concrete & Construction Chemistry, Swiss Federal Laboratories for Materials Science and Technology (Empa), 8600 Dübendorf, Switzerland
[c] Department of Structural Engineering, Norwegian University of Science and Technology (NTNU), 7491 Trondheim, Norway

ARTICLE INFO

ABSTRACT

Volume increase between the reactants and the products of alkali-silica reaction could reach up to 100%. Taking place inside the aggregates, ASR imposes internal pressure on the surrounding material. In the current paper, the possibility of crack growth due to such internal loading is studied. This study is done by employing a semi-analytical mechanical model comprising an elastic solution to a well-known Eshelby problem and a linear elastic fracture mechanics solution to a ring-shaped crack encircling a spheroidal inclusion. The proposed method implies the presence of pre-existing micro-fissures within the aggregate.

The study reveals the dependence of the crack growing potential on the spheroid's shape: the larger the ASR pocket - the longer crack opens. The two most critical shapes, causing the highest stress intensity factor and developing the longest crack, are a sphere and a spheroid with a 1/4 aspect ratio respectively. The size analysis of the problem suggests a critical spheroid's radius below which no crack growth is expected. For a chosen material properties and expansion value, such radius lies in the range between $0.1\,\mu m$ and $1\,\mu m$. Independently of the expansion value and the shape of the pocket of the ASR product, the developed crack length has a power-law dependence on the size of a spheroid.

All the theoretical predictions are confirmed by a numerical model based on the combination of the finite element method and the cohesive zone model.

1. Introduction

The alkali-silica reaction (ASR) in concrete is the reaction between SiO_2 contained in aggregates and alkalies coming from the cement paste [1]. Expanding ASR products accumulate within the aggregate leading to a build-up of stress, expansion of concrete and evolution of cracks. ASR causes substantial damage to the concrete infrastructure worldwide [2].

The formation of ASR products starts in the aggregate close to the interface with the cement paste. With ongoing reaction, the formation of ASR products continuously moves towards the interior of the aggregate. Fig. 1 shows three adjacent quartz grains in a reactive quartzite aggregate of a concrete doped with caesium nitrate [3]. The contact zone of the three grains is lined with a thin film of ASR products exhibiting a high back-scattering contrast due to the incorporation of caesium. Although the collective form of the ASR products reflects the one of the pre-existing cracks and voids as shown in Fig. 1, the newly formed ASR

products precipitate as clusters of alkali-silicate gel [4]. These newly formed clusters can be regarded as "pockets". They form between adjacent mineral grains within reactive aggregates close to the border with the cement paste [5,6]. The primary ASR product yields internal loading on aggregates leading to cracking. The resulting cracks originate in the aggregates and extend into cement paste. Crack openings could be much larger than the initial ASR product size and the openings of the pre-existing cracks. As reaction advances, the alkali front moves inwards the aggregates, producing more and more ASR sites. The newly formed cracks start to fill with the secondary ASR products.

The most widely reported hypothesis for the expansion of concrete caused by ASR is swelling of the ASR products due to the uptake of water - the so-called theory of imbibition or osmotic pressure [7–9]. Recent water uptake measurements on the synthetic ASR products, however, indicate a very limited water uptake [10]. This suggests that ASR expansion is not caused by the water-related swelling of the ASR products but by alternative mechanisms. Other proposed theories explaining
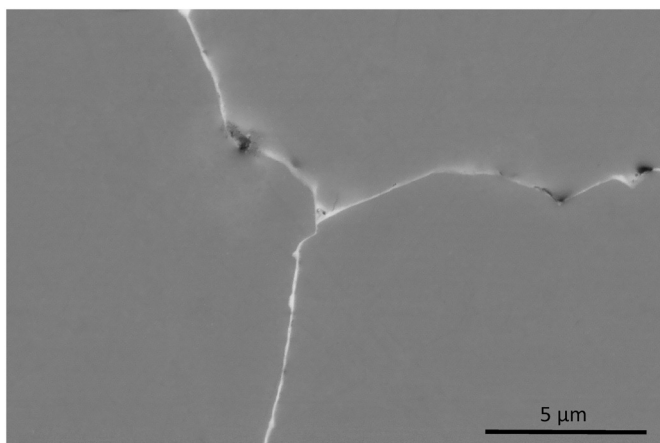

Fig. 1. Three adjacent quartz grains lined with a thin film of bright ASR products with a thickness between $50 - 300$ nm in a yet uncracked concrete aggregate. The brightness is caused by the doping of the concrete with caesium and its incorporation in the ASR products. Scanning electron image in the back-scattering mode adapted from [3].
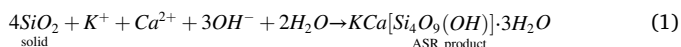
the ASR expansion mechanism include the theory of crystallisation pressure by Dron and colleagues [11,12], the theory of ion diffusion by Chatterji and Thaulow, Ichikawa and Miura, and Wang and Gillot [13–16], the theory of dispersion of gel by Jones [17] and the theory of electrical double-layer repulsion by Prezzi et al. and Rodrigues et al. [18,19]. Even though the underlying mechanism for expansion is not exactly known, it is clear that the formation of ASR products, which incorporates, in addition to SiO_2, also ions (K^+, Ca^{2+}, OH^-) and water from the pore solution, leads to an increase in solid volume. ASR products, commonly reported in the literature, precipitate as an amorphous gel. However, it has been shown that in addition to the amorphous ASR product, the one present in large cracks within aggregates could be crystalline [20–23].

The goal of this study is to verify the hypothesis if the microscopic ASR products could initiate cracks due to their expansion. If this is the case, the role of the shape and the size of an ASR pocket is to be investigated. First, the responsible chemical reaction is identified and the increase in the volume of the products over the reactants is computed. Then, a semi-analytical mechanical model for an expanding ASR pocket encircled by a pre-existing micro-crack is formulated. The crack extension is predicted for the ASR pockets of different sizes, shapes and expansion values. Finally, the predictions are verified by a numerical model.

2. Methods

2.1. Chemical reaction

A typical ASR formation reaction could be written as

$$\underset{\text{solid}}{4SiO_2} + K^+ + Ca^{2+} + 3OH^- + 2H_2O \rightarrow \underset{\text{ASR product}}{KCa[Si_4O_9(OH)]\cdot 3H_2O} \tag{1}$$

that describes the formation of an ASR product with molar ratios K/Si and Ca/Si of 0.25. These ratios correspond to the elemental ratios observed in ASR products in the field samples as well as to those observed in laboratory synthesised ASR products, although they vary to a certain extent [10,24–26]. All calculations presented here refer to the idealised composition given in Eq. (1).

Assuming quartz or amorphous SiO_2 as a silica source, it is possible to calculate the increase of solid volume if the ASR product is formed within the space originally occupied by SiO_2. Note that other species (K^+, Ca^{2+}, OH^-, and H_2O), needed to form ASR products, are assumed to diffuse into the aggregate from the cement pore solution, such that their

volume is not considered. Based on the molar volume of quartz (22.6 cm^3/mol), and the molar volume of the crystalline ASR product K-shlykovite, $KCa[Si_4O_9(OH)] \cdot 3H_2O$, of 183 cm^3/mol [27] (or 45.7 cm^3/mol if normalised to 1 silica: $K_{0.25}Ca_{0.25}[SiO_{2.25}(OH)_{0.25}] \cdot 0.75H_2O$) an increase in solid volume by a factor of two is obtained, and a ratio between the additional volume ($45.7 - 22.6 = 23.1$) and the initial volume is $23.1/22.6 \approx 1.0$, thus leading to 100% expansion. For amorphous ASR products, the molar volume has not been measured but based on the extensive analysis performed by Leemann and colleagues [23], the amorphous ASR product with a composition of $Na_{0.1}K_{0.2}Ca_{0.2}SiO_{2.3}(OH)_{0.1} \cdot 1.1H_2O$ indicates a similar or even higher volume increase (≈ 2.3) as for the crystalline ASR product. The duplication of the initial volume due to the precipitation of the ASR product could potentially lead to the formation of cracks within aggregates. This hypothesis was studied in detail based on a semi-analytical mechanical model of an inclusion-crack system within an infinite medium.

The generation of crystallisation pressures due to the over-saturation of the surrounding solution during the formation of ASR products cannot be excluded as a possible expansion mechanism. This direction is not further investigated in the present paper as no solution measurements are available, making a reliable estimation of maximum crystallisation pressures presently not possible.

2.2. Analytical model of expanding ASR pockets

The dependence of the possible crack growth on the size and the shape of ASR products is studied by exploring a semi-analytical mechanical model that consists of two components. The first one is a purely analytical model for an inclusion expanding within an infinite medium. The second one is a semi-analytical model of a ring-shaped crack encircling the previously described inclusion. The resulting model yields stress concentrations at the external crack tip that are used to evaluate the crack growth. A pocket of an ASR product is assumed to have an spheroidal shape since the latter comprises a wide range of shapes with central symmetry (e.g. spheres, oblate spheroids, disks, etc.).

The departing point of the analytical model is the Eshelby problem [28] that describes an expanding ellipsoidal inclusion embedded in an infinite medium. The term "inclusion" implies that its elastic properties differ from the ones of the matrix. The inclusion represents a single pocket of an ASR product surrounded by the aggregate. In this study, a spheroid is considered - a type of an ellipsoid with a circular cross-section. Here, a relatively small ASR pocket is assumed, which is positioned sufficiently far from the aggregate's boundary not to cause any mechanical influence, thus justifying the "infinite surrounding medium" condition. Given the known expansion of the inclusion, the elastic properties of the ASR product and the aggregate, their shapes and sizes, the stress and strain fields could be determined. The problem was solved by Eshelby [28,29] for general eigen strains. The solutions for the inclusion and the matrix are different. Later, Mura [30] provided explicit equations for the Eshelby tensor $\mathbb{S}$ for different shapes of an ellipsoid at the interior points. Ju and Sun [31,32] gave the first explicit formulas for computing the Eshelby tensor in the surrounding matrix. Healy [33] developed a MATLAB™ code with the Eshelby solution in 3D both inside and outside the inclusion.

A spheroidal inclusion with the semi-axis a and the equatorial radius r (shown in Fig. 2) is embedded in a matrix. Variation of the semi-axis a allows considering different geometries: 1) a sphere ($a = r$); 2) a needle ($a \gg r$); 3) a penny (or a disk) ($a \ll r$). The expansion is applied at the inclusion in the form of the eigenstrain ε_{eig} - a strain causing zero stress under no confinement. The eigenstrain is linked to the elastic strain ε_{el} as

$$\varepsilon = \varepsilon_{el} + \varepsilon_{eig} \tag{2}$$

where ε is the total strain. The volumetric expansion of the ASR product of 100% (introduced in Section 2.1) is applied in the form of the isotropic eigenstrain ε_{eig} of value one.
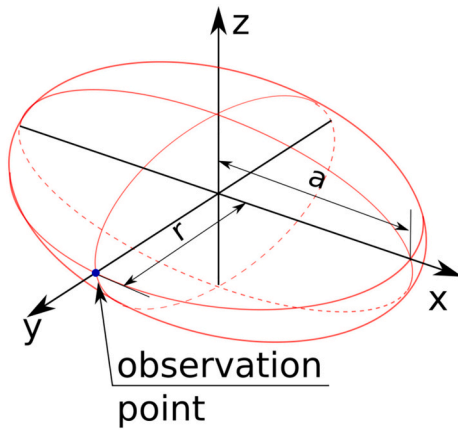
Fig. 2. Geometry of a spheroidal inclusion. Further in the text, stresses are evaluated either in the observation point or along the *y*-axis.

The matrix is an infinite body with the remote stress $\boldsymbol{\sigma}^0$ or strain $\boldsymbol{\varepsilon}^0$ applied at infinity. In the current study, a stress-free body with $\boldsymbol{\sigma}^0$ and $\boldsymbol{\varepsilon}^0$ equal to zero is assumed. The effect of external loading on the ASR was previously studied by several authors [e.g. 34–36].

The solution for the strain and stress inside the inclusion is given by Ju and Sun [32]

$$\begin{aligned} \boldsymbol{\varepsilon} &= \boldsymbol{\varepsilon}^0 + \mathbb{S} : \boldsymbol{\varepsilon}_{eig} \\ \boldsymbol{\sigma} &= \boldsymbol{\sigma}^0 + \mathbb{C}^0[\mathbb{S} - \mathbb{I}] : \boldsymbol{\varepsilon}_{eig} \end{aligned} \tag{3}$$

where $\mathbb{S}$ is the 4th-order Eshelby tensor for the interior points, $\mathbb{C}^0$ the matrix stiffness tensor and $\mathbb{I}$ the identity tensor. The particular property of the Eshelby problem is that the stress and strain fields at the interior points are uniform and the Eshelby tensor $\mathbb{S}$ is independent of the position within the inclusion.

Oppositely, for the corresponding fields outside the inclusion, the strain and the stress at a point depend on the position of the latter:

$$\begin{aligned} \boldsymbol{\varepsilon}(\mathbf{x}) &= \boldsymbol{\varepsilon}^0 + \mathbb{G}(\mathbf{x}) : \boldsymbol{\varepsilon}_{eig} \; \mathbb{G}(\mathbf{x}) : \boldsymbol{\varepsilon}_{eig} \\ \boldsymbol{\sigma}(\mathbf{x}) &= \boldsymbol{\sigma}^0 + \mathbb{C}^0 \, \mathbb{G}(\mathbf{x}) : \boldsymbol{\varepsilon}_{eig} \end{aligned} \tag{4}$$

where $\mathbb{G}(\mathbf{x})$ is a 4th-order Eshelby tensor for the exterior points.

Explicit formulas for the components of $\mathbb{S}$ and $\mathbb{G}(\mathbf{x})$, available in [32,33], yield the values of $\boldsymbol{\varepsilon}$ and $\boldsymbol{\sigma}$ at any point of space.

2.3. Semi-analytical model with a ring-shaped crack

Griffith [37] in his fundamental work showed that the material strength at the macro-scale is largely affected by the presence of microscopic flaws. For an expanding inclusion, to grow a crack from its surface, there should be an initial micro-fissure that would facilitate the crack propagation. a higher expansion would be required if such an inclusion would be surrounded by a sound material with no flaws in it. Pre-existing defects in the form of microcracks are common in aggregates [38].

A crack is added to the Eshelby problem as shown in Fig. 3. It has the shape of a flat ring in the *yz*-plane. While the inner crack tip lays exactly on the equator of the spheroid, the outer one extends by the distance *l*. *r* and *R* denote the internal and external crack radii correspondingly. An additional *y′*-axis was introduced for computation purposes: it is a *y*-axis with the origin shifted to the surface of the spheroid. The crack is opening in mode I. Keeping the expansion value fixed, a different alignment of a crack would reduce the probability of its extension.

According to the adopted model, the inclusion is always expanding as a solid body. When the crack extends, the ASR product does not flow inside. Therefore this model represents the ASR product in its mature stage. Accounting for the gel fluidity would require an enriched
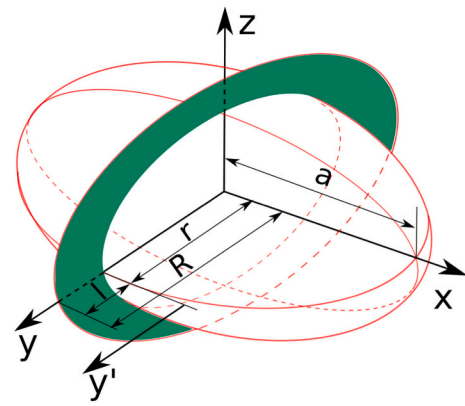

Fig. 3. Spheroid with the pre-existing disk-shaped crack in the *yz*-plane.

analytical model including mass conservation and pressure redistribution.

Aggregates are composed of a brittle material that fractures abruptly without undergoing significant softening. Such behaviour is well reproduced by the linear elastic fracture mechanics (LEFM) that serves as a base for the further analytical developments. The internal load $\varepsilon_{eig}=1$ is based on the expansive potential of the ASR product (see Section 2.1). Such a high expansion induces large strains that could not be sustained by the aggregate material. Instead, it would yield such second-order effects as micro-cracking around the inclusion and alteration of the LEFM-based crack shape and length. Predicting such behaviour is a challenging task. Here, a first-order qualitative prediction is aimed.

To evaluate the crack growth, one has to know K_I - the stress intensity factor (SIF) in mode I for the external crack tip. The principle of superposition states that applying $\boldsymbol{\sigma}(\mathbf{x})$ on the crack faces is similar to loading the cracked body with the loads that cause $\boldsymbol{\sigma}(\mathbf{x})$ in the absence of a crack [39]. To find K_I, the problem of a crack loaded by a spheroidal inclusion is replaced by a crack whose faces are loaded by the stresses caused by the expanding inclusion in the absence of the crack. The latter ones are known from the Eshelby solution.

Literature has few analytical solutions for computing K_I for ring-shaped cracks under simple loading (e.g. [40]). Unfortunately, a solution for a general stress distribution is not available. Instead, this problem could be solved using weight functions, as proposed by Bueckner and Rice [41,42]. These authors suggested using the known crack face displacement $u(l, x)$ and the known stress intensity factor $K_I{}^0$ for a symmetrical load system on a cracked body to compute unknown K_I for any other symmetrical load system. The equation for SIF reads as

$$K_I = \int_0^l \sigma(y')h(l, y')dy' \tag{5}$$

where $h(l, y')$ is a weight function defined as

$$h(l, y') = H\frac{\partial u}{\partial l} \Big/ K_I{}^0 \tag{6}$$

In Eqs. (5) and (6), *l* is the crack length equal to the difference between the external and internal radii $(R - r)$, *H* is a material parameter, $\sigma(y')$ is the stress distribution along the crack plane in the unflawed body under the load associated to K_I. The integration is carried out along the crack surface only. Fett and Rizzi [43] computed weight functions for a ring-shaped crack by the interpolating procedure. The latter is the reason for the solution being "semi-analytical". The weight function for the outer crack tip reads as

$$h(l, y')\sqrt{l} = \frac{2}{\sqrt{\pi(1 - y'/l)(l/r + 1)}} \left(\frac{1 + y'/r}{\sqrt{2 + l/r + y'/r}} - \frac{1 - \sqrt{y'/l}}{\sqrt{l/r + 2}} \right) \tag{7}$$

Plugging Eq. (7) and the stresses from Eq. (4) into Eq. (5) and

integrating it numerically results in the required values of K_I. A similar approach was previously used by Iskhakov et al. [44] within a multi-scale model.

2.4. Numerical validation

Analytical and semi-analytical predictions are validated through the numerical modelling. Two components of the final solution are verified. The first component is the elastic stress in the inclusion's surroundings in the absence of a crack. The second component is the actual crack radius for different inclusion shapes and sizes. The numerical model is based on the finite element method (FEM). All the simulations are performed using the open-source parallel FE library Akantu [45,46, akantu.ch].

The geometry used for the numerical model is shown in Fig. 4. It comprises one-quarter of the full space. Symmetry over the xz- and xy-planes is established by imposing zero out-of-plane displacements. The simulated block comprises one-quarter of the inclusion-matrix system. The equatorial radius of the spheroid is $1\,\mu m$, while the dimensions of the full block are $20 \times 20 \times 20\,\mu m^3$. The behaviour of the bulk materials (the aggregate and the inclusion) is linear elastic. The loading is prescribed at the inclusion in the form of the isotropic eigenstrain $\varepsilon_{eig}=1$ that represents a 100% volumetric expansion of the ASR product.

For verification of the developed crack radius, the crack plane is added to the FE model along the yz plane. The discontinuity is modelled by cohesive elements that are inserted along the pre-defined plane at the beginning of the simulation. The cohesive zone approach yields to dissipation of the fracture energy by the interface (or cohesive) elements placed between the neighbouring solid elements (see Fig. 5a). When two solid elements are being pulled apart, a cohesive element in-between resists by generating the inwards traction whose amplitude depends on the opening displacement value. Cohesive elements represent the non-linear process zone (or cohesive zone) at the crack tip, as originally proposed by Barenblatt and Dugdale [47,48].
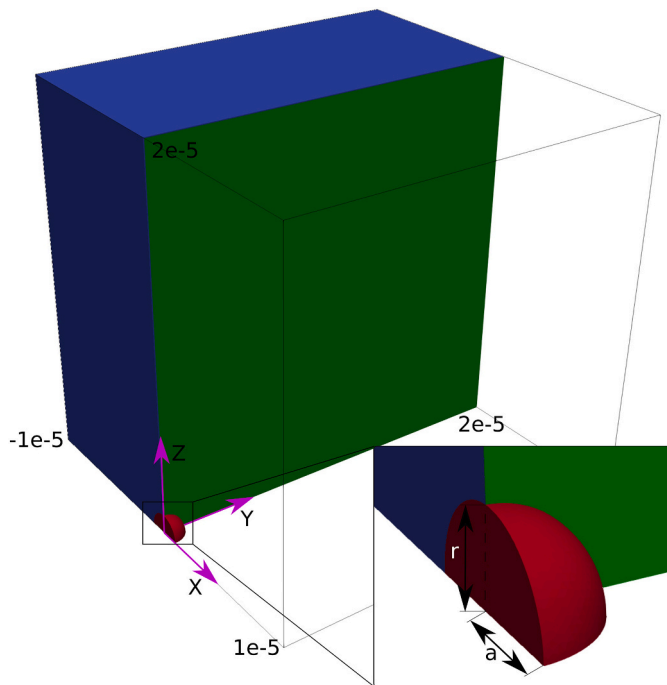
The behaviour of cohesive elements is stipulated through the traction-separation law. For the current study, a bi-linear traction-sep-aration law, shown in Fig. 5b, is employed. For the cohesive opening δ below the elastic limit δ_0, a cohesive element behaves in a linear elastic manner. The initial elastic opening of a cohesive element is a numerical artefact: ideally, the interface should be fully rigid up to the point where it reaches the tensile strength σ_t and softening starts. To minimise the artificial effect of pre-inserted cohesive elements on the behaviour of the bulk material, the elastic opening δ_0 should be kept very small, so that the initial stiffness of the cohesive element is higher than the one of the bulk material. After the traction T reaches the material strength in tension σ_t, it starts to decrease linearly reproducing material softening. The latter takes place up to a moment when the opening reaches its critical value δ_c. Then the element is fully broken. If the loading is removed while the element is in the softening stage ($\delta < \delta_c$), its behaviour becomes elastic again within the window $0 \leq \delta \leq \delta_{max}$. Under compression, cohesive elements behave elastically with a penalty coefficient α_p. Opening of a cohesive element dissipates energy E_{dis}. The maximum value that can be dissipated upon reaching the critical opening δ_c equals the fracture energy G_c according to

$$\delta_c = 2\frac{G_c}{\sigma_t} \tag{8}$$

where G_c could be computed from the fracture toughness K_{IC} as

$$G_c = \frac{K_{IC}^2}{E} \tag{9}$$

where E is the Young's modulus of the surrounding material. It is assumed that no friction is present and only normal opening of cohesive elements takes place.

While the LEFM-based semi-analytical solution assumes that the material undergoes brittle failure, the cohesive zone model suggests that it undergoes softening that is contained in the process zone next to the crack tip. The length of this zone, l_z, depends on the adopted model. According to Hillerborg and colleagues [49], it can be estimated as

$$l_z = \frac{EG_c}{\sigma_t^2} \tag{10}$$

To make the cohesive zone model match the LEFM solution, the process zone l_z should be big enough to accommodate several finite elements, but smaller than any other model length scale (the size of the inclusion, the crack, and the domain). For an inclusion of $1\,\mu m$ radius and a domain of $20\,\mu m$ size, a $0.2\,\mu m$ cohesive zone was chosen. The crack plane was meshed with the element size of $0.03\,\mu m$ that allowed having several elements within the cohesive zone. In Eq. (10), E and G_c are material properties, while σ_t is treated as a calibration parameter. To make l_z equal to $0.2\,\mu m$, the tensile strength σ_t was assigned 4.5 GPa (see Table 1). Such a high value is adopted to make the cohesive zone model comply with the principles of LEFM. The values of σ_t, δ_0 and δ_c are given in Table 1.

3. Results

The theoretical predictions of stresses and crack radii are made for different inclusion shapes and sizes. The theory is then validated by comparing it with the numerical model.

3.1. Stresses in the bulk

To compute the stresses, material properties given in Table 1 are used. Due to the unavailability of the mechanical properties of the amorphous ASR product, those of the crystalline state are taken.

The analytical solution for the stresses inside and outside the inclusion is given in Fig. 6. Directions x, y and z coincide with the principal stress directions. Stresses at the interior points are independent of the

Fig. 4. Geometry of the numerical model used for the verification study. Red colour corresponds to the ASR product, blue to the surrounding aggregate, green to the predefined crack plane. The second half of the aggregate is omitted for visualisation of the crack plane. The dimensions are given in meters. (For interpretation of the references to colour in this figure legend, the reader is referred to the web version of this article.)
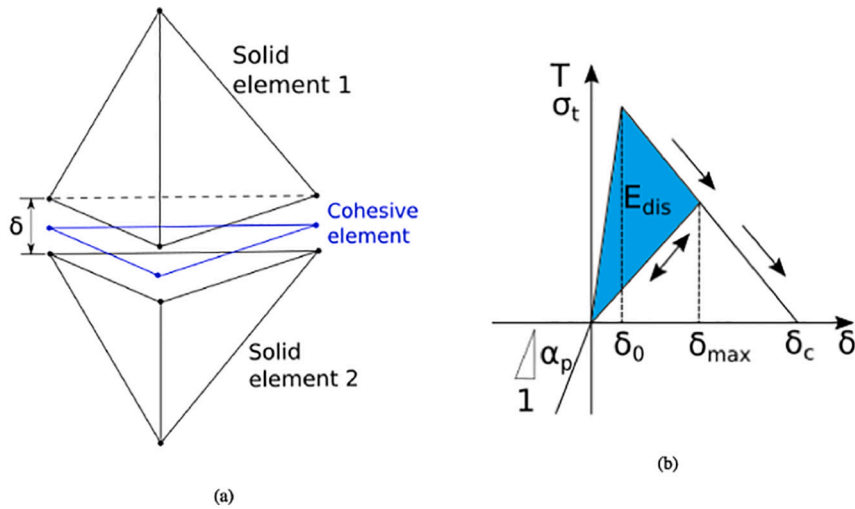
Fig. 5. a) A sketch of a first-order 2D cohesive element between 3D solid elements. b) Illustration of the bi-linear cohesive law.

Table 1
Material properties of the ASR product and the aggregate matrix, and parameters of the bi-linear cohesive law. * Based on the micro-indentation tests by Leemann and Lura [25]. † Taken from [50].

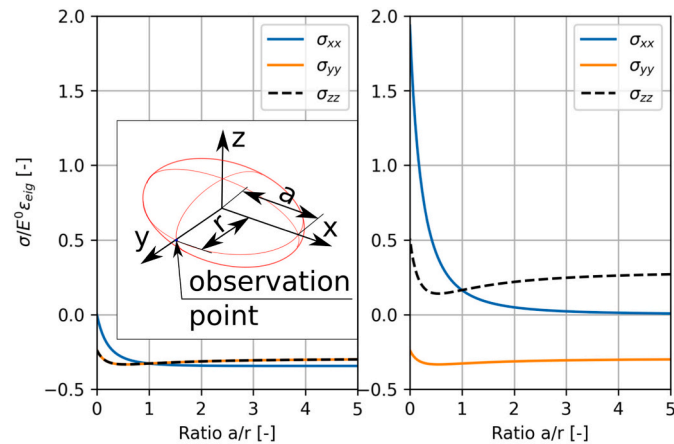| Material properties	ASR product*	Aggregate †	Cohesive material
Young's modulus E, [GPa]	10	60	–
Poisson's ratio ν, [−]	0.3	0.3	–
Fracture toughness K_{IC}, [MPa · $m^{1/2}$]	–	2	–
Fracture energy G_c, [J/m²]	–	–	66.7
Tensile strength σ_t, [MPa]	–	–	$4.5 \cdot 10^3$
Elastic opening δ_0, [ηm]	–	–	1
Critical opening δ_c, [ηm]	–	–	29.6

Fig. 6. Stresses inside (on the left) and outside the inclusion (on the right) at the observation point for a varying inclusion's shape. Stresses are normalised by a product of the matrix's Young's modulus E^0 and the eigenstrain scalar ε_{eig}. The semi-axis a is normalised by the equatorial radius r.

point's position. Stresses in the matrix are plotted at the intersection point between the y-axis and the surface of the spheroid (see the observation point in Fig. 2). The semi-axis a is varied from almost zero to five times the equatorial radius r, changing from a penny to a sphere and finally to a needle. Stresses inside the inclusion are always compressive, becoming hydrostatic ($\sigma_{xx} = \sigma_{yy} = \sigma_{zz}$) in the spherical configuration. When approaching the disk limit, the stress in the direction normal to

the disk plane tends towards zero. The stress state in the matrix is different. While the stress in the y-direction is still compressive, the other two stresses are either null or tensile. This creates necessary premises for the crack appearance. In the spherical setup, the tensile stresses in the x- and y-directions are equal that makes any plane passing through the y-axis suitable for the crack growth. In the penny-shape limit ($a/r \rightarrow 0$), σ_{xx} intensifies making the yz-plane preferable for a crack to grow. Since the gel inclusions are expected to have a flat shape, the analysis is limited to the cases when a/r changes from zero to one.

the analytical solution for stresses along the y-axis for three different shapes of the inclusion is plotted in Fig. 7. Although the disk has a tensile stress at the border much larger than the one of a sphere, it decays much faster. For a spherical configuration ($a = r$), the stress drops with the rate of r^3/y^3, which matches a well-known analytical solution by Timoshenko and Goodier [51], p. 417. A particularity of the Eshelby solution is its size independence: both the small and the large inclusions will generate similar stress and strain fields under the same expansion value.

The numerical solution for the stress along the y-axis fairly matches the analytical predictions. A comparison between the two sets of results is plotted in Fig. A14 of Appendix. At this stage, no crack is present in the simulation. The only difference between the two methods is observed at the boundary, where FEM cannot represent the stress singularity for oblate shapes. The numerical solution could be improved by mesh refinement. The stress decay further from the inclusion surface is perfectly resolved.
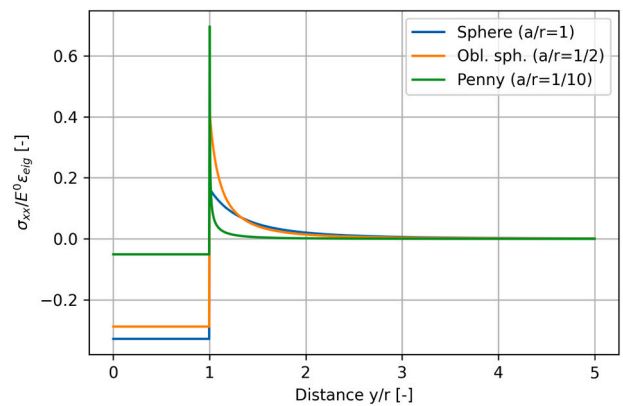

Fig. 7. Stress σ_{xx} for three different inclusion shapes plotted along the y-axis. Its value is normalised by a product of the matrix's Young's modulus E^0 and the eigenstrain scalar ε_{eig}. The distance y is normalised by the equatorial radius r.

3.2. Crack radius

The crack is added to the numerical problem employing cohesive elements. The parameters of the cohesive law are listed in Table 1. To have a small l_z and preserve the fracture energy G_c, the tensile strength σ_t had to be assigned a high value and the critical opening δ_c had to be adjusted.

Expansion of the inclusion leads to the concentration of stresses at the crack tip. The intensity of this concentration is characterised by the stress intensity factor. The analytical solution for K_I depending on the spheroid's shape and the crack radius are plotted in Fig. 8. The equatorial radius of the inclusion in this plot equals 1 μm. K_I normalised by the fracture toughness K_{IC} serves as an indicator for crack growth. While the values of K_I/K_{IC} above one suggest that the crack will extend, a strict equality indicates the crack radius at which growth will cease. Cracking due to the ASR is happening in a quasi-static regime. The expansion value of 100% is not applied at once but is gradually increased. The process of crack growth is illustrated for the case of a spherical inclusion in Fig. 9. The cracking starts at a value that is lower than the final load. More specifically, the first crack extension happens when K_I at the peak of the curve becomes equal to K_{IC} (point 1 of Fig. 9). After the first crack growth event, any further infinitesimal increase in the load would lead to an increase in the crack length (point 2). At all times, the stress intensity factor K_I is strictly equal to the fracture toughness K_{IC}, and the crack propagation is stable. Finally, the load reaches its final value, and the crack growth arrests at point 3.

All the curves in Fig. 8 have a unimodal distribution shape. At the extreme values of R, zero and ∞, K_I tends towards zero. In physical terms, it means that for a crack to grow, a pre-existing fissure of a finite length must exist. Otherwise, the problem transitions from being toughness-controlled to strength-controlled [52,53]. Overcoming material strength in the absence of micro-fissures would require higher expansion values of the ASR pocket. In contrast, a sufficiently large size of the pre-existing crack encircling the inclusion facilitates its further growth.

The curves in Fig. 8 are ascending up to the K_I peak value and later descend to zero. Such behaviour of K_I is not typical: most of the classical fracture mechanical problems result in either monotonously growing or reducing K_I, e.g. tension applied at the infinity or tensile force pair applied at the centre of a penny-shaped crack. One may wonder why in the case of the expanding inclusion K_I has a peak, while in the case of a remote tensile load it does not. The difference in K_I profiles stems from the different nature of loads. For the remote tensile load, the crack tip always "feels" the tensile stress applied at infinity. For the expanding inclusion, the matrix stresses in the absence of the crack are not
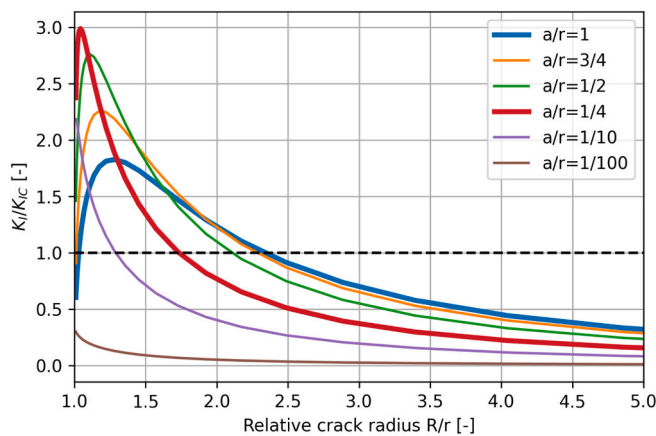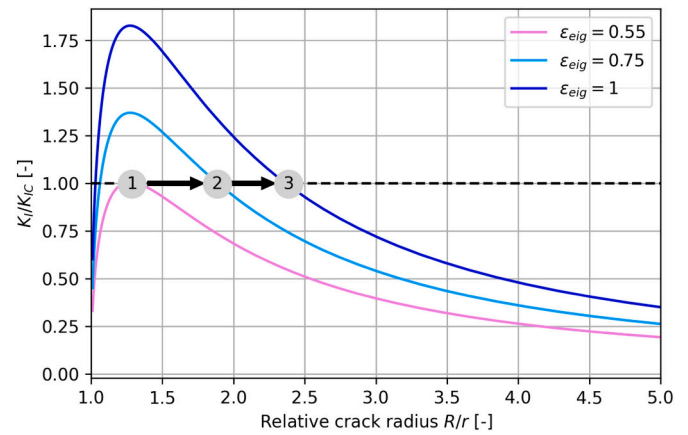

Fig. 9. Illustration of the crack growth process around a spherical inclusion. Point 1 denotes the lowest value of expansion at which crack extension begins. Point 2 corresponds to some intermediate expansion value at which crack propagates in a stable mode ($K_I = K_{IC}$). Crack growth stops upon reaching the final ε_{eig} at the point 3.

constant. For simplicity, a spherical case is considered. In Fig. 10, the normalised stress σ_{xx} and the stress intensity factor K_I are plotted along the distance y' given in logarithmic scale. The stress intensity factor was computed for the geometry where the crack size l equals the distance y'. The stress is constant up to $y'/r = 10^{-3}$ after which it starts to drop. While the stress is constant, K_I is monotonously growing (similar to the remote tension case). When the stress reduces, so does K_I, which results in a peak.

The K_I peak position and its height vary for different shapes of the inclusion. The highest K_I corresponds to an oblate spheroid with an aspect ratio $a/r = 1/4$ that makes it the most critical case for high fracture toughness. A sphere ($a/r = 1$) has a lower peak value, but its developed crack length is the largest. Consequently, a sphere and a 1/4-spheroid are the two most critical geometries with regards to the K_I intensity and the developed crack length correspondingly.

For the current equatorial radius of a spheroid $r = 1 \mu m$, any aspect ratio $1/10 \leq a/r \leq 1$ leads to fracture growth. Flattening the shape of the inclusion would reduce its potential to grow a crack. For instance, a penny with thickness $a = 0.01 \mu m$ is not expected to develop a crack. The maximum crack radius for all possible spheroids with $1 \mu m$ radius is $2.35 \mu m$ that is more than twice as big as the ASR pocket itself.

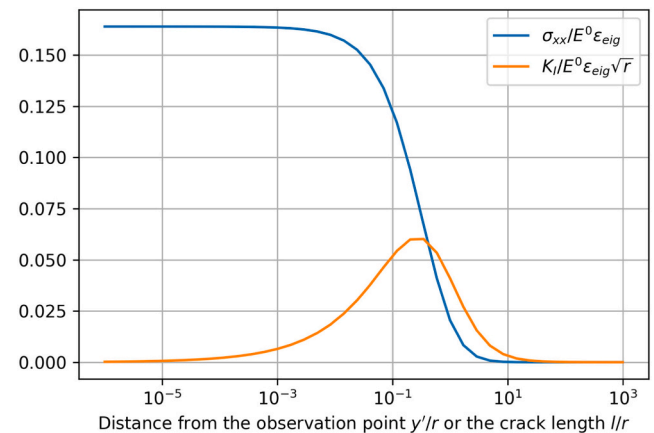Although the stress solution of the Eshelby problem does not depend

Fig. 8. K_I/K_{IC} depending on the aspect ratio of the spheroid a/r and the external crack radius R/r for a spheroid with the fixed equatorial radius $r = 1 \mu m$ under the expansion of 100%.

Fig. 10. σ_{xx} along y'-axis in an unflawed configuration and K_I for a crack of length $l = y'$. Values are normalised by a product of the matrix's Young's modulus E^0 and the eigenstrain scalar ε_{eig}. An extra normalisation term $1/\sqrt{r}$ is applied to K_I. The distances y' and l are normalised by the equatorial radius r.

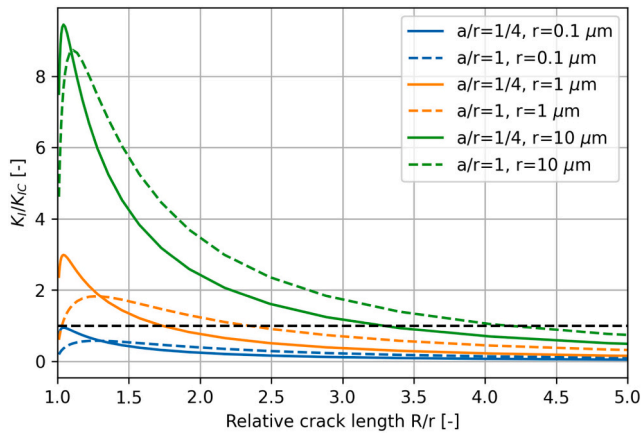**Fig. 11.** K_I/K_{IC} for a sphere and 1/4 spheroid of different radii and a constant expansion of 100%.
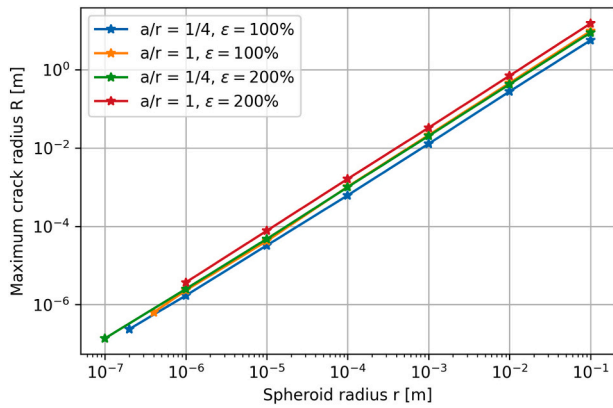

Fig. 12. Developed crack radii for spheroidal inclusions of different sizes under different expansion values plotted in log-log scale.

Fig. 13. Final values of damage in the numerical simulations for three spheroids with the radius $1\,\mu m$ and the expansion of 100%. The dotted lines denote semi-analytical predictions of the developed crack radii presented in Fig. 8. The dimensions are given in meters.

on the size of the inclusion, the solution for the stress intensity factor does. This is demonstrated in Fig. 11. The two most critical shapes (a sphere and a 1/4 spheroid) of different radii were tested: $0.1\,\mu m$, $1\,\mu m$, and $10\,\mu m$. The same expansion value was applied. One can observe a gradual increase in both the peak SIF value and the developed crack length for bigger inclusions. This allows us to conclude that the size of the ASR pocket has a direct effect on the crack propagation: larger ASR inclusions have a higher chance to damage the surrounding aggregate and thus cause a longer crack. Another important observation is that, irrespective of its shape, an inclusion of $0.1\,\mu m$ size or smaller does not trigger crack growth. This observation suggests that there is a critical value of the spheroid's radius below which no crack extension will happen for the expansion values of 100% and the chosen material properties. This critical radius lays in the range between $0.1\,\mu m$ and $1\,\mu m$.

To study how the inclusion size is related to the developed crack radius, an additional parametric study was performed results of which are presented in Fig. 12. Two previously highlighted shapes (a sphere and a 1/4-spheroid) were increased in size from hundreds of nanometers to a few centimetres and the corresponding crack radii were measured. Such a wide range was chosen for purely illustrative purposes and does not have any physical implications. The expansion values of 100% and 200% were applied. The results are plotted in a log-log scale. The developed crack radius shows a power-law dependence on the inclusion size. The power-law reveals an exponent of 4/3. The results suggest that the same power-law exponent holds for different expansion values.
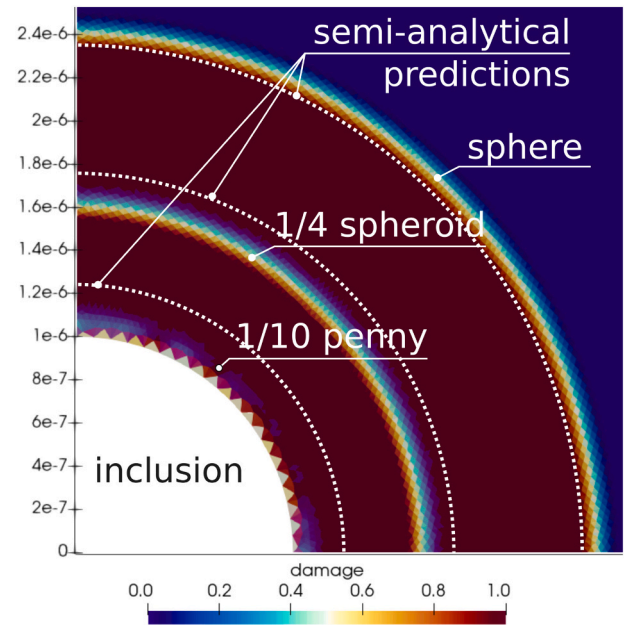
Numerical validation of the analytical solution is given in Fig. 13. Here, white dotted lines represent the semi-analytical predictions for three spheroids, while the coloured background comprises three numerical crack profiles. The final positions of the numerical cracks can be interpreted through the damage colours: brown corresponds to the fully damaged cohesive elements, blue is for the intact ones. Rainbow-coloured regions correspond to the cohesive zones at the external crack radii. The radius of the crack next to a sphere is about $2.4\,\mu m$ that is almost equal to the analytically predicted radius of $2.35\,\mu m$. For a 1/4-spheroid, the numerically-grown crack measures $1.6\,\mu m$ that is 8.5% smaller than the analytical value of $1.75\,\mu m$. Finally, a penny has not developed a crack and just slightly opened a rim of elements while its analytical prediction is $1.27\,\mu m$. The reason for the underdeveloped crack is believed to be the interference coming from the inclusion that is too close-by. Except for this last case, the numerical model fairly reproduces the semi-analytical predictions.

4. Conclusions

In this study, the potential of ASR pockets of different sizes and shapes to cause cracking of surrounding aggregates due to their volume increase of 100% was estimated. For this, a semi-analytical model consisting of the expanding spheroidal inclusion and a ring-shaped crack encircling it was employed. The inclusion here represents a pocket of an ASR product at its mature solid state. A prerequisite for such a model is the presence of pre-existing fissures, which are abundant in rocks. First, the stresses in the matrix are computed by an analytical solution. Later, the product of the computed stresses and the specific weight function is integrated over the surface of a crack to obtain the stress intensity factor for mode I. The latter characterises the crack potential to grow. The distance at which the stress intensity factor normalised by the fracture toughness equals one renders the developed crack length.

The resulting solution strongly depends on the inclusion's shape and size. Flat shapes concentrate higher tensile stresses on their sharp edges than the bulging ones. At the same time, these stresses decay much faster further away from the inclusion. While the stress intensity factor for mode I is the highest for an oblate spheroid with an aspect ratio of 1/4,

the longest crack is caused by a spherical shape. It makes 1/4-spheroid and a sphere the two most critical shapes, either for reaching high values of the fracture toughness or for causing the longest crack.

The size of the inclusion plays a crucial role on the crack growing potential. For an inclusion of $1\,\mu m$ radius under the expansion of 100%, all spheroidal shapes with aspect ratios above 1/10 are likely to grow a crack around. Flatter shapes would cause either shorter cracks ($R/r \leq 1.25$) or no crack at all. There is a critical inclusion radius in the range between $0.1\,\mu m$ and $1\,\mu m$ below which no crack growth is expected for the current combination of K_{IC} and ε_{eig}. Consistently, an increase in the inclusion's size yields higher values of K_I and longer cracks.

Further increase in the inclusion size, as well as in the expansion value, suggests a power-law dependence between the radius of a spheroid and the developed crack radius. Independent of the spheroidal shape or the expansion value, the power-law exponent is about 4/3.

The results of the analytical and semi-analytical predictions were confirmed by the numerical model. For verification of the stresses in the bulk in the absence of the crack, a purely elastic finite element model was assembled. For validating the predicted crack length, this model was enriched with cohesive elements. Both the elastic stresses and the crack lengths obtained numerically have a good match with the semi-analytical results.

CRediT authorship contribution statement

E.R. Gallyamov: Conceptualization, Methodology, Software, Writing - original draft, Writing - review & editing, Validation, Visualization, Formal analysis. A. Leemann: Conceptualization, Writing - original draft, Writing - review & editing. B. Lothenbach: Conceptualization, Writing - original draft, Writing - review & editing. J.F. Molinari: Supervision, Conceptualization, Methodology, Writing - review & editing, Funding acquisition.

Declaration of competing interest

The authors declare that they have no known competing financial interests or personal relationships that could have appeared to influence the work reported in this paper.

Acknowledgements
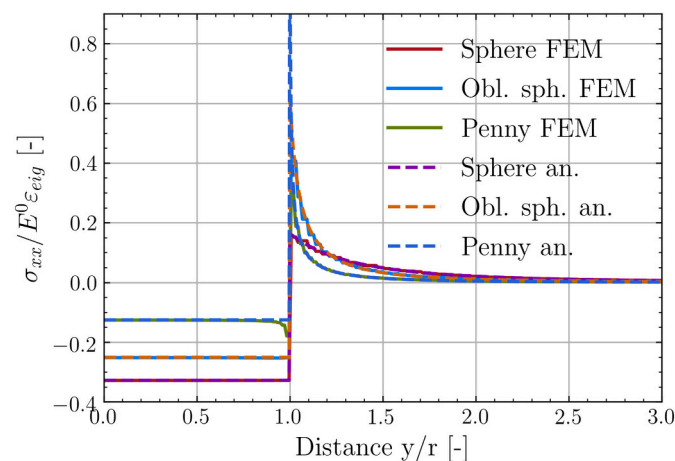
Appendix A. Supplementary plots

Fig. A14. Comparison of the stress σ_{xx} along the *y*-axis from the analytical model and FE simulation.

References

[1] R.N. Swamy, Alkali-silica reaction in concrete, ISBN 978-0-203-20033-9. URL, Blackie and Son ; Taylor and Francis e-Library, Glasgow, England; New York, New York, 2003. OCLC: 1132080496, https://www.taylorfrancis.com/books/02030 36638.

[2] R. Charlwood, I. Sims, A review of the effectiveness of strategies to manage expansive chemical reactions in dams and hydro projects, in: Swelling Concr. Dams Hydraul. Struct, 2017, pp. 3–39.

[3] A. Leemann, Impact of different alkalis on concrete expansion due to ASR, in: Proceedings of the 16 th International Conference on Alkali-Aggregate Reaction in Concrete volume 1, 2021.

[4] F. Gaboriaud, A. Nonat, D. Chaumont, A. Craievich, Aggregation processes and formation of silico-calco-alkaline gels under high ionic strength, J. Colloid Interface Sci. 253 (1) (Sept. 2002) 140–149, https://doi.org/10.1006/jcis.2002.8522. https://linkinghub.elsevier.com/retrieve/pii/S00219797029 8522X.

[5] A. Leemann, B. Münch, The addition of caesium to concrete with alkali-silica reaction: implications on product identification and recognition of the reaction sequence, URL, Cem. Concr. Res. 120 (June 2019) 27–35, https://doi.org/10.1016/j.cemconres.2019.03.016, https://linkinghub.elsevier.com/retrieve/pii/S0008884619300730.

[6] A. Leemann, T. Katayama, I. Fernandes, M.A.T.M. Broekmans, Types of alkali–aggregate reactions and the products formed, URL, Proc. Inst. Civ. Eng. Constr. Mater 169 (3) (June 2016) 128–135, https://doi.org/10.1680/jcoma.15.00059, http://www.icevirtuallibrary.com/doi/10.1680/jcoma.15.00059.

[7] S. Diamond, ASR - another look at mechanisms, in: Proceedings of the 8th International Conference on Alkali-Aggregate Reaction, Kyoto, Japan, 1989.

[8] L.S.D. Glasser, Osmotic pressure and the swelling of gels, URL, Cem. Concr. Res. 9 (4) (July 1979) 515–517, https://doi.org/10.1016/0008-8846(79)90050-4, https://www.sciencedirect.com/science/article/pii/0008884679900504.

[9] A.B. Poole, Alkali-silica reactivity mechanisms of gel formation and expansion, in: Proceedings of the 9th International Conference on Alkali-Aggregate Reaction, London (England) volume 104, Concrete Society Publications CS, 1992, pp. 782–789. Issue: 1.

[10] Z. Shi, G. Geng, A. Leemann, B. Lothenbach, Synthesis, characterization, and water uptake property of alkali-silica reaction products, URL, Cem. Concr. Res. 121 (July 2019) 58–71, https://doi.org/10.1016/j.cemconres.2019.04.009, https://linkinghub.elsevier.com/retrieve/pii/S0008884619301139.

[11] R. Dron, Thermodynamique de la réaction alcali-silice, Bull. Liaison Lab Ponts Chaussées (166) (1990).

[12] R. Dron, F. Brivot, T. Chaussadent, Mécanisme de la réaction alcali-silice, Bull. Lab. Ponts Chaussees (1998) 61–68.

[13] S. Chatterji, Mechanisms of alkali- silica reaction and expansion, in: Proceedings of the 8th International Conference on Alkali-Aggregate Reaction, Kyoto, Japan, 1989.

[14] S. Chatterji, N. Thaulow, Some fundamental aspects of alkali-silica reaction, in: Proc., 11th AAR Inter. Conf., Québec, Canada, 2000, pp. 21–29.

[15] T. Ichikawa, M. Miura, Modified model of alkali-silica reaction, URL, Cem. Concr. Res. 37 (9) (Sept. 2007) 1291–1297, https://doi.org/10.1016/j.cemconres.2007.06.008, https://www.sciencedirect.com/science/article/pii/S0008884607001329.

[16] H. Wang, J.E. Gillott, Mechanism of alkali-silica reaction and the significance of calcium hydroxide, URL, Cem. Concr. Res. 21 (4) (July 1991) 647–654, https://doi.org/10.1016/0008-8846(91)90115-X, https://www.sciencedirect.com/science/article/pii/000888469190115X.

[17] T.N. Jones, New interpretation of alkali-silica reaction and expansion mechanisms in concrete, Chem. Ind. (1988) 40–44.

[18] M. Prezzi, P.J. Monteiro, G. Sposito, The alkali–silica reaction: part I. Use of the double-layer theory to explain the behavior of reaction-product gels, ACI Mater. J. 94 (1) (1997) 10–17.

[19] F.A. Rodrigues, P.J. Monteiro, G. Sposito, The alkali-silica reaction: the surface charge density of silica and its effect on expansive pressure, Cem. Concr. Res. 29 (4) (1999) 527–530. Publisher: Elsevier.

[20] W.F. Cole, C.J. Lancucki, Products formed in an aged concrete the occurrence of okenite, URL, Cem. Concr. Res. 13 (5) (Sept. 1983) 611–618, https://doi.org/10.1016/0008-8846(83)90049-2, https://www.sciencedirect.com/science/article/pii/0008884683900492.

[21] R. Dähn, A. Arakcheeva, P. Schaub, P. Pattison, G. Chapuis, D. Grolimund, E. Wieland, A. Leemann, Application of micro X-ray diffraction to investigate the reaction products formed by the alkali–silica reaction in concrete structures, URL, Cem. Concr. Res. 79 (Jan. 2016) 49–56, https://doi.org/10.1016/j.cemconres.2015.07.012, https://www.sciencedirect.com/science/article/pii/S0008884615002094.

[22] L.De Ceukelaire, The determination of the most common crystalline alkali-silica reaction product, Mater. Struct. 24 (3) (May 1991) 169–171, https://doi.org/10.1007/BF02472981. ISBN 978-0-7918-0153-6, http://link.springer.com/10.1007/BF02472981.

[23] A. Leemann, Z. Shi, J. Lindgård, Characterization of amorphous and crystalline ASR products formed in concrete aggregates, URL, Cem. Concr. Res. 137 (Nov. 2020), 106190, https://doi.org/10.1016/j.cemconres.2020.106190, https://linkinghub.elsevier.com/retrieve/pii/S0008884620304324.

[24] T. Iskhakov, C. Giebson, J.J. Timothy, H.M. Ludwig, G. Meschke, Deterioration of concrete due to ASR: experiments and multiscale modeling, URL, Cem. Concr. Res. 149 (Nov. 2021) 106575, https://doi.org/10.1016/j.cemconres.2021.106575, https://www.sciencedirect.com/science/article/pii/S0008884621002246.

[25] A. Leemann, P. Lura, E-modulus of the alkali–silica-reaction product determined by micro-indentation, URL, Constr. Build. Mater. 44 (July 2013) 221–227, https://doi.org/10.1016/j.conbuildmat.2013.03.018, https://linkinghub.elsevier.com/retrieve/pii/S0950061813002237.

[26] Z. Shi, S. Park, B. Lothenbach, A. Leemann, Formation of shlykovite and ASR-P1 in concrete under accelerated alkali-silica reaction at 60 and 80 C, URL, Cem. Concr. Res. 137 (Nov. 2020), 106213, https://doi.org/10.1016/j.cemconres.2020.106213, https://www.sciencedirect.com/science/article/pii/S0008884620304622.

[27] G. Geng, Z. Shi, A. Leemann, K. Glazyrin, A. Kleppe, D. Daisenberger, S. Churakov, B. Lothenbach, E. Wieland, R. Dähn, Mechanical behavior and phase change of alkali-silica reaction products under hydrostatic compression, URL, Acta Crystallogr. Sect. B: Struct. Sci. Cryst. Eng. Mater. 76 (4) (Aug. 2020) 674–682, https://doi.org/10.1107/S205252062000846X, https://scripts.iucr.org/cgi-bin/paper?S205252062000846X.

[28] J.D. Eshelby, The elastic field outside an ellipsoidal inclusion, URL, Proc. R. Soc. Lond. A 252 (1271) (Oct. 1959) 561–569, https://doi.org/10.1098/rspa.1959.0173, https://royalsocietypublishing.org/doi/10.1098/rspa.1959.0173.

[29] J.D. Eshelby, The determination of the elastic field of an ellipsoidal inclusion, and related problems, URL, Proc. R. Soc. Lond. A 241 (1226) (Aug. 1957) 376–396, https://doi.org/10.1098/rspa.1957.0133, https://royalsocietypublishing.org/doi/10.1098/rspa.1957.0133.

[30] T. Mura, Micromechanics of Defects in Solids, 1987.

[31] J.W. Ju, L.Z. Sun, A novel formulation for the exterior-point Eshelby's tensor of an ellipsoidal inclusion, URL, J. Appl. Mech. 66 (2) (June 1999) 570–574, https://doi.org/10.1115/1.2791090, https://asmedigitalcollection.asme.org/appliedmechanics/article/66/2/570/445956/A-Novel-Formulation-for-the-ExteriorPoint-Eshelbys.

[32] J.W. Ju, L.Z. Sun, Effective elastoplastic behavior of metal matrix composites containing randomly located aligned spheroidal inhomogeneities. Part I: micromechanics-based formulation, Int. J. Solids Struct. (2001) 19.

[33] D. Healy, Elastic field in 3D due to a spheroidal inclusion—MATLAB code for Eshelby's solution, Comput. Geosci. 35 (10) (Oct. 2009) 2170–2173, https://doi.org/10.1016/j.cageo.2008.11.012. https://linkinghub.elsevier.com/retrieve/pii/S0098300409001356.

[34] C.F. Dunant, K.L. Scrivener, Effects of uniaxial stress on alkali–silica reaction induced expansion of concrete, Cem. Concr. Res. 42 (3) (Mar. 2012) 567–576, https://doi.org/10.1016/j.cemconres.2011.12.004. https://linkinghub.elsevier.com/retrieve/pii/S0008884611003267.

[35] C. Larive, Apports combinés de l'expérimentation et de la modélisation à la compréhension de l'alcali-réaction et de ses effets mécaniques, l'École Nationale des Ponts et Chaussées, 1997. PhD thesis.

[36] S. Multon, F. Toutlemonde, Effect of applied stresses on alkali–silica reaction-induced expansions, URL, Cem. Concr. Res. 36 (5) (May 2006) 912–920, https://doi.org/10.1016/j.cemconres.2005.11.012, https://linkinghub.elsevier.com/retrieve/pii/S0008884605002838.

[37] A.A. Griffith, The phenomena of rupture and flow in solids, URL, Philos. Trans. R. Soc. Lond. A 221 (582-593) (Jan. 1921) 163–198, https://doi.org/10.1098/rsta.1921.0006, https://royalsocietypublishing.org/doi/10.1098/rsta.1921.0006.

[38] M.H. Anders, S.E. Laubach, C.H. Scholz, Microfractures: a review, URL, J. Struct. Geol. 69 (Dec. 2014) 377–394, https://doi.org/10.1016/j.jsg.2014.05.011, https://www.sciencedirect.com/science/article/pii/S0191814114001151.

[39] H. Petroski, J. Achenbach, Computation of the weight function from a stress intensity factor, Eng. Fract. Mech. 10 (2) (Jan. 1978) 257–266, https://doi.org/10.1016/0013-7944(78)90009-7. https://linkinghub.elsevier.com/retrieve/pii/0013794478900097.

[40] H. Tada, P.C. Paris, G.R. Irwin, The Stress Analysis of Cracks Handbook, 3rd ed, ASME Press, New York, 2000. ISBN 978-0-7918-0153-6.

[41] H.F. Bueckner, Novel principle for the computation of stress intensity factors, URL, Z. Angew. Math. Mech. 50 (9) (Sept. 1970), https://trid.trb.org/view/3976.

[42] J.R. Rice, Some remarks on elastic crack-tip stress fields, URL, Int. J. Solids Struct. 8 (6) (June 1972) 751–758, https://doi.org/10.1016/0020-7683(72)90040-6, https://linkinghub.elsevier.com/retrieve/pii/0020768372900406.

[43] T. Fett, G. Rizzi, in: Weight Functions and Stress Intensity Factors for Ring-shaped Cracks, 2007, p. 48.

[44] T. Iskhakov, J.J. Timothy, G. Meschke, Expansion and deterioration of concrete due to ASR: micromechanical modeling and analysis, Cem. Concr. Res. 115 (Jan. 2019) 507–518, https://doi.org/10.1016/j.cemconres.2018.08.001. https://linkinghub.elsevier.com/retrieve/pii/S0008884618301509.

[45] Akantu, URL, https://akantu.ch/, Aug. 2021.

[46] N. Richart, J. Molinari, Implementation of a parallel finite-element library: test case on a non-local continuum damage model, URL, Finite Elem. Anal. Des. 100 (Aug. 2015) 41–46, https://doi.org/10.1016/j.finel.2015.02.003, https://linkinghub.elsevier.com/retrieve/pii/S0168874X15000153.

[47] G. Barenblatt, The mathematical theory of equilibrium cracks in brittle fracture, URL, in: Advances in Applied Mechanics 7, Elsevier, 1962, pp. 55–129, https://doi.org/10.1016/S0065-2156(08)70121-2, https://linkinghub.elsevier.com/retrieve/pii/S0065215608701212.

[48] D. Dugdale, Yielding of steel sheets containing slits, URL, J. Mech. Phys. Solids 8 (2) (May 1960) 100–104, https://doi.org/10.1016/0022-5096(60)90013-2, https://linkinghub.elsevier.com/retrieve/pii/0022509660900132.

[49] A. Hillerborg, M. Modéer, P.-E. Petersson, Analysis of crack formation and crack growth in concrete by means of fracture mechanics and finite elements, URL, Cem. Concr. Res. 6 (6) (Nov. 1976) 773–781, https://doi.org/10.1016/0008-8846(76)90007-7, https://linkinghub.elsevier.com/retrieve/pii/0008884676900077.

[50] H. Alehossein, J.N. Boland, Strength, toughness, damage and fatigue of rock, in: Structural Integrity and Fracture: Proceedings of the International Conference, SIF 2004, 2004, p. 8.

[51] S. Timoshenko, J.N. Goodier, Theory of Elasticity, URL, 3 edition, McGraw-Hill, 1951.

[52] Z.P. Bažant, Size effect in blunt fracture: concrete, rock, metal, URL, J. Eng. Mech. 110 (4) (Apr. 1984) 518–535, https://doi.org/10.1061/(ASCE)0733-9399(1984)110:4(518), http://ascelibrary.org/doi/10.1061/%28ASCE%290733-9399%281984%29110%3A4%28518%29.

[53] R.O. Ritchie, The conflicts between strength and toughness, Nat. Mater. 10 (11) (Nov. 2011) 817–822, https://doi.org/10.1038/nmat3115. https://www.nature.com/articles/nmat3115.